AIAA JOURNAL
Vol. 48, No. 11, November 2010

Patched Characteristic Interface Conditions for High-Order Multiblock Aeroacoustic Computation

Edward Peers,* Xin Zhang,† and Jae Wook Kim‡
University of Southampton, Southampton, England SO17 1BJ, United Kingdom

DOI: 10.2514/1.J050130

A patched grid technique is proposed with the aim of increasing the flexibility and efficiency of high-order finite difference schemes for multiblock computational aeroacoustics. The patched characteristic interface conditions allow arbitrarily positioned nonmatching grid points along each side of the internal block boundaries. The work extends the characteristic interface conditions originally proposed to treat the problem of grid singularity associated with structured grids and high-order finite difference schemes. A simple method of generalizing the original characteristic interface conditions theory for arbitrary block coordinate alignments is also outlined. The new interface condition is implemented into a high-order computational aeroacoustics code to solve either the Euler or Navier–Stokes equations. The patch algorithm makes use of a high-order optimized interpolation method to approximate the characteristic convection terms at corresponding locations along the block interface. The result is an interface condition that provides better management of cell distribution in the computational domain while at the same time providing a treatment to the grid singularity problem associated with complex geometries. Several test cases are used to demonstrate the flexibility of the new interface condition and to investigate various parameters. The computed results are shown to be in excellent agreement with exact solutions.

Nomenclature

C	=	vortex strength factor
c	=	speed of sound
c_p	=	specific heat at constant pressure
c_v	=	specific head at constant volume
$\boldsymbol{E}, \boldsymbol{F}, \boldsymbol{G}$	=	inviscid flux vectors
$\boldsymbol{E_v}, \boldsymbol{F_v}, \boldsymbol{G_v}$	=	viscous flux vectors
e_t	=	total energy per unit mass
f	=	function
J	=	Jacobian matrix
K	=	interpolation stencil interval
$\boldsymbol{L}$	=	characteristic wave term
M	=	Mach number
N	=	number of stencil points
$\bar{\boldsymbol{P}}$	=	characteristic transformation matrix
p	=	pressure
$\boldsymbol{Q}$	=	vector of conserved variables
R	=	vortex core radius
S_j	=	optimized interpolation coefficients
t	=	time
U, V, W	=	contravariant velocities
u, v, w	=	Cartesian velocity components
x, y, z	=	Cartesian coordinate directions
γ	=	ratio of specific heats
δ	=	interpolation offset
ϵ	=	pressure pulse amplitude
$\boldsymbol{\lambda}$	=	vector of characteristic convection speeds
ξ, η, ζ	=	generalized coordinate directions
ρ	=	density

Presented as Paper 2009-3112 at the 15th AIAA/CEAS Aeroacoustics Conference, Miami, FL, 11–13 May 2009; received 12 August 2009; revision received 1 July 2010; accepted for publication 18 July 2010.

*Research Fellow, Aeronautics and Astronautics, School of Engineering Sciences. Member AIAA.

†Professor, Aeronautics and Astronautics, School of Engineering Sciences. Associate Fellow AIAA.

‡Lecturer, Aeronautics and Astronautics, School of Engineering Sciences. Member AIAA.

I. Introduction

THE field of computational aeroacoustics (CAA) is concerned with the accurate numerical prediction of aerodynamically generated noise as well as its propagation and far-field characteristics. CAA methods are generally different to computational fluid dynamics (CFD) methods due to the disparity between the length scales associated with the sound field and the mean flow. Whilst many CFD problems can be adequately simulated using low-order methods, the use of high-order finite difference schemes (FDS) are required for CAA applications due to their superior accuracy and resolution characteristics [1]. High-order finite difference methods require high quality structured grids. However, practical CAA problems, such as those associated with aircraft noise, are often concerned with complex geometries making the generation of smooth high quality grids extremely challenging. Often grid skew (the abrupt change in the gradient along a grid line) is unavoidable, leading to the issue of grid singularity. The grid singularity problem causes a discontinuity in the grid metrics at the singular point when approximated by the high-order FDS due to the discrepancy between left- and right-hand limits of the gradients.

Another problem is that body-fitted structured grids often lead to a poor distribution of cells in the domain due to the requirement of continuous grid lines (i.e. the one-to-one constraint in a multiblock computation). Usually, different regions of the domain demand different grid resolution characteristics. For example, in a direct simulation the grid requirements in the source near field, which is usually viscous, will be different to that in the Euler region where resolution of the propagating acoustic waves is important. When integral techniques, such as the Ffowcs-Williams and Hawkings equation [2], are employed, one does not require a fine mesh throughout the entire domain, and the mesh can often be coarsened away from the source. Thus, the one-to-one grid constraint may lead to either poor computational efficiency, or a compromise in the grid quality. Therefore the challenge is to develop CAA methods so that the high-order FDSs can be used to solve more complex problems.

Overset grid methods [3–5] are a popular approach that have made the use of high-order FDSs more applicable to complex geometries. In overset, or overlapping, approaches a body fitted curvilinear structured grid is overlaid on to a homogeneous isotropic grid making generation of a structured grid throughout the entire domain less complex. However, the mesh coupling method between the two grid types is nontrivial leading to complex implementation and additional computational cost. Moreover, the challenge of avoiding grid singularity within the body fitted grid is still an issue.

One method to treat the grid singularity problem is to adopt a multiblock approach whereby the computational domain is structured so that the block interfaces coincide with lines of grid skew. Some form of interface condition is then needed between the block boundaries. Possible candidates for such interface conditions have been derived based on the simultaneous approximation term penalty method [6] and also on the characteristic form of the governing equations [7]. Kim and Lee [7] derived characteristic interface conditions (CICs) for solving the Navier–Stokes equations on multiblock curvilinear grids. In this method one-sided differencing is applied along the block interfaces so that the numerical stencil does not cross points of grid singularity. Interface conditions, based on the characteristic form of the Navier-Stoke equations, are then imposed along the block interfaces to ensure proper interblock communication. An extended version of the CICs to allow various metric alignments between blocks was presented by Sumi et al. [8]. This method offers a solution to the problem of grid skew; however the constraint of connected grid lines between blocks limits the efficiency of the computation of complex geometries.

Patched grid (also known as nonconformal or staggered grid) methods allow one to locally refine the grid in a multiblock computation by allowing an arbitrary number and distribution and of grid points on either side of the block boundaries. This enables an improved distribution of grid points throughout the domain. The patched grid method is normally associated with finite-volume methods since the treatment of a discontinuous differencing stencil and communication of the flow variables across the patched interface is not straightforward for finite difference methods. However, the CICs present a solution to these problems and thus an opportunity to develop a patched CICs method [9].

In this work generalized patched CICs are presented for CAA application. The patched grid method extends the CICs by allowing nonmatching grid points along the block boundaries. This is achieved by using a high-order optimized interpolation scheme along the block interfaces to interpolate the characteristic variables between the nonmatching grid points. The proposed method provides a solution to the grid singularity problem and provides more control of the grid resolution characteristics improving the overall computational efficiency. In this paper the original CICs are reviewed and a simple method is presented to obtain the generalized CICs for use with arbitrary multiblock configurations. Key numerical details are outlined and the implementation procedure for the new interface condition is described. This is followed by validation of the method by solving several benchmark test cases.

The rest of this paper is organized as follows: In Sec. II, the characteristic form of the governing equations is revisited. In Sec. III the generalized CICs are presented and in Sec. IV the patched CICs method is outlined. In Sec. V details of the numerical algorithms are provided. Results to three test cases are presented in Sec. VI followed by a summary in Sec. VII.

II. Governing Equations in Characteristic Form

The governing equations are either the unsteady compressible Euler or Navier–Stokes equations. For completeness the Navier–Stokes equations will be considered here. In generalized coordinates the Navier–Stokes equations can be expressed as

$$\frac{\partial \hat{\boldsymbol{Q}}}{\partial t}+\frac{\partial(\hat{\boldsymbol{E}}-\hat{\boldsymbol{E}}_{\boldsymbol{v}})}{\partial \xi}+\frac{\partial(\hat{\boldsymbol{F}}-\hat{\boldsymbol{F}}_{\boldsymbol{v}})}{\partial \eta}+\frac{\partial(\hat{\boldsymbol{G}}-\hat{\boldsymbol{G}}_{\boldsymbol{v}})}{\partial \zeta}=0 \tag{1}$$

where the caret indicates the transformed properties. In Eq. (1) $\boldsymbol{E}_{\boldsymbol{v}}$, $\boldsymbol{F}_{\boldsymbol{v}}$, $\boldsymbol{G}_{\boldsymbol{v}}$ are the viscous flux terms which are zero for the Euler equations. The viscous flux vectors are described in detail in [10]. The vectors of the conservative variables and the Euler fluxes in the generalized coordinates are given by

$$\hat{\boldsymbol{Q}}=\boldsymbol{Q}/J, \qquad \hat{\boldsymbol{E}}=(\xi_x\boldsymbol{E}+\xi_y\boldsymbol{F}+\xi_z\boldsymbol{G})/J,$$
$$\hat{\boldsymbol{F}}=(\eta_x\boldsymbol{E}+\eta_y\boldsymbol{F}+\eta_z\boldsymbol{G})/J, \qquad \hat{\boldsymbol{G}}=(\zeta_x\boldsymbol{E}+\zeta_y\boldsymbol{F}+\zeta_z\boldsymbol{G})/J \tag{2}$$

and the corresponding vectors in Cartesian coordinates are given by

$$\begin{aligned}\boldsymbol{Q}&=(\rho,\rho u,\rho v,\rho w,\rho e_t)^T,\\ \boldsymbol{E}&=(\rho u,\rho u^2+p,\rho vu,\rho wu,(\rho e_t+p)u)^T,\\ \boldsymbol{F}&=(\rho v,\rho uv,\rho v^2+p,\rho wv,(\rho e_t+p)v)^T,\\ \boldsymbol{G}&=(\rho w,\rho uw,\rho vw,\rho w^2+p,(\rho e_t+p)w)^T\end{aligned} \tag{3}$$

where the total energy per unit mass is defined by $e_t=p/[(\gamma-1)\rho]+(u^2+v^2+w^2)/2$ and $\gamma=c_p/c_v$ is the ratio of specific heats equal to 1.4 for air. The Jacobian of transformation J and the grid metrics are given by

$$J=1/[x_\xi(y_\eta z_\zeta-y_\zeta z_\eta)+x_\eta(y_\zeta z_\xi-y_\xi z_\zeta)+x_\zeta(y_\xi z_\eta-y_\eta z_\xi)]$$

with

$$\begin{pmatrix}\xi_x & \xi_y & \xi_z\\ \eta_x & \eta_y & \eta_z\\ \zeta_x & \zeta_y & \zeta_z\end{pmatrix}=J\begin{pmatrix}y_\eta z_\zeta-y_\zeta z_\eta & z_\eta x_\zeta-z_\zeta x_\eta & x_\eta y_\zeta-x_\zeta y_\eta\\ y_\zeta z_\xi-y_\xi z_\zeta & z_\zeta x_\xi-z_\xi x_\zeta & x_\zeta y_\xi-x_\xi y_\zeta\\ y_\xi z_\eta-y_\eta z_\xi & z_\xi x_\eta-z_\eta x_\xi & x_\xi y_\eta-x_\eta y_\xi\end{pmatrix} \tag{4}$$

The governing equations can be transformed into quasi-linear wave equations so that the flow properties can be classified into physical wave modes. Equation (1) can be written in characteristic form in the direction normal to the interface where ξ, without loss of generality, has a constant value:

$$\frac{\partial \boldsymbol{R}}{\partial t}+\bar{\boldsymbol{\lambda}}\frac{\partial \boldsymbol{R}}{\partial \xi}=\boldsymbol{S}_C \tag{5}$$

The terms in Eq. (5) are defined as

$$\delta\boldsymbol{R}=\bar{\boldsymbol{P}}^{-1}\delta\boldsymbol{Q}, \qquad \bar{\boldsymbol{\lambda}}\frac{\partial \boldsymbol{R}}{\partial \xi}=\bar{\boldsymbol{P}}^{-1}\left(\xi_x\frac{\partial \boldsymbol{E}}{\partial \xi}+\xi_y\frac{\partial \boldsymbol{F}}{\partial \xi}+\xi_z\frac{\partial \boldsymbol{G}}{\partial \xi}\right) \tag{6}$$

and the source term $\boldsymbol{S}_c$ is given by

$$\begin{aligned}\boldsymbol{S}_C=J\bar{\boldsymbol{P}}^{-1}\Bigg\{&\frac{\partial \hat{\boldsymbol{E}}_{\boldsymbol{v}}}{\partial \xi}+\frac{\partial \hat{\boldsymbol{F}}_{\boldsymbol{v}}}{\partial \eta}+\frac{\partial \hat{\boldsymbol{G}}_{\boldsymbol{v}}}{\partial \zeta}-\left[\boldsymbol{E}\frac{\partial}{\partial \xi}\left(\frac{\xi_x}{J}\right)\right.\\ &\left.+\boldsymbol{F}\frac{\partial}{\partial \xi}\left(\frac{\xi_y}{J}\right)+\boldsymbol{G}\frac{\partial}{\partial \xi}\left(\frac{\xi_z}{J}\right)+\frac{\partial \hat{\boldsymbol{F}}}{\partial \eta}+\frac{\partial \hat{\boldsymbol{G}}}{\partial \zeta}\right]\Bigg\}\end{aligned} \tag{7}$$

where $\bar{\boldsymbol{P}}^{-1}$ is a matrix that transforms the conservative variables into the characteristic variables. $\bar{\boldsymbol{P}}^{-1}$ and its inverse matrix $\bar{\boldsymbol{P}}$ diagonalize the flux-Jacobian matrices in the direction normal to the interface. The diagonalizing procedure is described in detail in [11,12] and the transformation matrices are given in the Appendix. The characteristic differential variables and the corresponding convection speeds are represented as

$$\delta\boldsymbol{R}=\left(\tilde{\xi}_x\delta s+\delta\tilde{V}_x,\tilde{\xi}_y\delta s+\delta\tilde{V}_y,\tilde{\xi}_z\delta s+\delta\tilde{V}_z,\frac{\delta p}{\rho c}+\delta\tilde{U},\frac{\delta p}{\rho c}-\delta\tilde{U}\right)^T \tag{8}$$

$$\begin{aligned}\bar{\lambda}(\text{diag})=(&U,U,U,U+c\sqrt{\xi_x^2+\xi_y^2+\xi_z^2},U\\ &-c\sqrt{\xi_x^2+\xi_y^2+\xi_z^2})^T\end{aligned} \tag{9}$$

where

$$\delta s=\delta\rho-\frac{\delta p}{c^2} \tag{10}$$

$$\delta\tilde{V}_x = \tilde{\xi}_z\delta v - \tilde{\xi}_y\delta w, \qquad \delta\tilde{V}_y = \tilde{\xi}_x\delta w - \tilde{\xi}_z\delta u$$
$$\delta\tilde{V}_z = \tilde{\xi}_y\delta u - \tilde{\xi}_x\delta v \tag{11}$$

In Eqs. (8) and (9) the tilde indicates a quantity normalized by $|\nabla\xi|$, c is the speed of sound. The contravariant velocity and its differential are given by

$$U = \xi_x u + \xi_y v + \xi_z w, \qquad \delta\tilde{U} = \tilde{\xi}_x\delta u + \tilde{\xi}_y\delta v + \tilde{\xi}_z\delta w \tag{12}$$

Equation (5) represents the physical (entropy, vorticity, and acoustic) waves with different convection speeds normal to the interface given by Eq. (9). This is used to derive the CICs which are presented in the next section.

III. Generalized Characteristic Interface Conditions

The CICs were proposed by Kim and Lee [7] to solve the problem of grid singularity caused by skewed grid lines. The idea was decompose the computational domain along the skewed grid lines and to treat each block in isolation in regards to the numerical discretization so that the differencing stencils do not cross the block interfaces. Thus the singularity problem is avoided, but there is no longer any communication between adjacent blocks. Therefore, interface conditions based on the characteristic form of the governing equations were proposed to communicate the incoming and outgoing characteristic waves between the unconnected adjacent blocks in a strict manner. They are derived from the relation that the primitive variables and their time derivatives on the left and right side of the interface should be equal such that

$$(\rho^L, \boldsymbol{v}^L, p^L) = (\rho^R, \boldsymbol{v}^R, p^R), \qquad \partial_t(\rho^L, \boldsymbol{v}^L, p^L) = \partial_t(\rho^R, \boldsymbol{v}^R, p^R) \tag{13}$$

The above relation can be expressed in terms of the characteristic variables to derive the CICs. In the original work of Kim and Lee the interface conditions were demonstrated for a ξ constant block boundary where the grid metrics in each block are aligned. In this situation the relative alignment of the block metrics can be expressed as

$$\nabla\tilde{\boldsymbol{\xi}}^L = \nabla\tilde{\boldsymbol{\xi}}^R \tag{14}$$

where

$$\nabla\tilde{\boldsymbol{\xi}} = \nabla\boldsymbol{\xi}/|\nabla\boldsymbol{\xi}| = (\tilde{\xi}_x, \tilde{\xi}_y, \tilde{\xi}_z)^T \tag{15}$$

In this case Eq. (13) can be expressed in terms of the characteristic variables by

$$\frac{\partial \boldsymbol{R}^L}{\partial t} = \frac{\partial \boldsymbol{R}^R}{\partial t} \tag{16}$$

and if the convection term in Eq. (5) is given as

$$\boldsymbol{L} = \bar{\lambda}\frac{\partial \boldsymbol{R}}{\partial \xi}$$

then Eq. (16) can then be represented as

$$\boldsymbol{L}^L - \boldsymbol{S}_C^L = \boldsymbol{L}^R - \boldsymbol{S}_C^R \tag{17}$$

The characteristic waves can be easily classified as outgoing or incoming by the sign of their convection speeds, and so waves passing between the block interfaces can be compensated for in each block. The decision of which should be chosen is based on the sign of the convection speed. If Eq. (14) is satisfied then the interface conditions can be summarized as

$$\begin{aligned} L_m^L &= L_m^R - S_{Cm}^R + S_{Cm}^L \quad \text{if } \lambda_m^L/|\lambda_m^L| \\ &= \lambda_m^R/|\lambda_m^R| \le 0, \quad \text{and} \quad \nabla\tilde{\boldsymbol{\xi}}^L = \nabla\tilde{\boldsymbol{\xi}}^R \\ L_m^R &= L_m^L - S_{Cm}^L + S_{Cm}^R \quad \text{if } \lambda_m^L/|\lambda_m^L| \\ &= \lambda_m^R/|\lambda_m^R| \ge 0, \quad \text{and} \quad \nabla\tilde{\boldsymbol{\xi}}^L = \nabla\tilde{\boldsymbol{\xi}}^R \end{aligned} \tag{18}$$

where the subscript m represents the components of a vector $m = 1, \ldots, 5$.

For practical applications it is useful to consider the arbitrary arrangement of blocks leading to various alignments of the grid metrics along the interface. In this situation Eq. (14) and therefore Eq. (17) are not always satisfied. The general case was considered by Sumi et al. [8] who outlined a generalized approach to imposing the original interface conditions along arbitrary block interfaces. The approach led to additional matrices and steps leading to a more complex implementation. In this work it is shown that the generalized characteristic interface conditions (GCICs) can simply be derived from the initial theory by assessing the contravariant velocity U, the convection speed $\bar{\boldsymbol{\lambda}}$, and the relative coordinate directions at the interface.

For general metric configurations between blocks $\nabla\tilde{\boldsymbol{\xi}}^L = \pm\nabla\tilde{\boldsymbol{\xi}}^R$ and for each case there are two possible grid metric alignment combinations. The GCICs for the subsonic ($U < c$) case can be summarized by Fig. 1 which shows all the four possible combinations of the grid metric alignments between blocks and the resulting characteristic wave convection directions. In Fig. 1 the hollow arrows correspond to the characteristic convection term $\boldsymbol{L}$ that should be compensated by another on the adjacent block. Cases (a) and (b) correspond to the original interface conditions defined by Eq. (18) since $\nabla\tilde{\boldsymbol{\xi}}^L = \nabla\tilde{\boldsymbol{\xi}}^R$, whereas in cases (c) and (d) alternative interface conditions are required since $\nabla\tilde{\boldsymbol{\xi}}^L = -\nabla\tilde{\boldsymbol{\xi}}^R$. The dilemma is how to identify which of the four cases in Fig. 1 applies to the interface. This can be determined by evaluating the index of the grid coordinate along the interface of the left and right-hand blocks, i.e., to determine if $\xi_{\min}^L$, or $\xi_{\max}^L$, and if $\xi_{\min}^R$, or $\xi_{\max}^R$, as shown in Fig. 1.

The additional interface conditions for the subsonic cases (c) and (d) corresponding to $\nabla\tilde{\boldsymbol{\xi}}^L = -\nabla\tilde{\boldsymbol{\xi}}^R$ can be expressed as

(c) $\xi_{\max}^L \to \xi_{\max}^R$, $\nabla\tilde{\boldsymbol{\xi}}^L = -\nabla\tilde{\boldsymbol{\xi}}^R$:

$$\begin{aligned} &L_m^L = L_m^R - S_{Cm}^R + S_{Cm}^L \quad \text{if } \lambda_m^L/|\lambda_m^L| = \lambda_m^R/|\lambda_m^R| \le 0, \\ &m = 1, 2, 3. \qquad L_5^L = L_4^R - S_{C4}^R + S_{C5}^L, \\ &L_m^R = L_m^L - S_{Cm}^L + S_{Cm}^R \quad \text{if } \lambda_m^L/|\lambda_m^L| = \lambda_m^R/|\lambda_m^R| \ge 0, \\ &m = 1, 2, 3. \qquad L_5^R = L_4^L - S_{C4}^L + S_{C5}^R \end{aligned} \tag{19}$$

(d) $\xi_{\min}^L \to \xi_{\min}^R$, $\nabla\tilde{\boldsymbol{\xi}}^L = -\nabla\tilde{\boldsymbol{\xi}}^R$:

$$\begin{aligned} &L_m^L = L_m^R - S_{Cm}^R + S_{Cm}^L \quad \text{if } \lambda_m^L/|\lambda_m^L| = \lambda_m^R/|\lambda_m^R| \le 0, \\ &m = 1, 2, 3. \qquad L_4^L = L_5^R - S_{C5}^R + S_{C4}^L, \\ &L_m^R = L_m^L - S_{Cm}^L + S_{Cm}^R \quad \text{if } \lambda_m^L/|\lambda_m^L| = \lambda_m^R/|\lambda_m^R| \ge 0, \\ &m = 1, 2, 3. \qquad L_4^R = L_5^L - S_{C5}^L + S_{C4}^R \end{aligned} \tag{20}$$

For the supersonic ($U > c$) case each component of $\boldsymbol{L}$ has a convection speed in the downstream direction so that the supersonic CICs can be expressed as

$$L_m^D = L_m^U - S_{Cm}^U + S_{Cm}^D \quad \text{if } U > c, \qquad m = 1, \ldots, 5 \tag{21}$$

where $\boldsymbol{L}^U$ and $\boldsymbol{L}^D$ represent the upstream and downstream terms, respectively. Thus a complete set of generalized CICs has been obtained by simple analysis of the convection speeds, the contravariant velocity, and relative grid metric directions, and they are summarized by Eqs. (18–21).

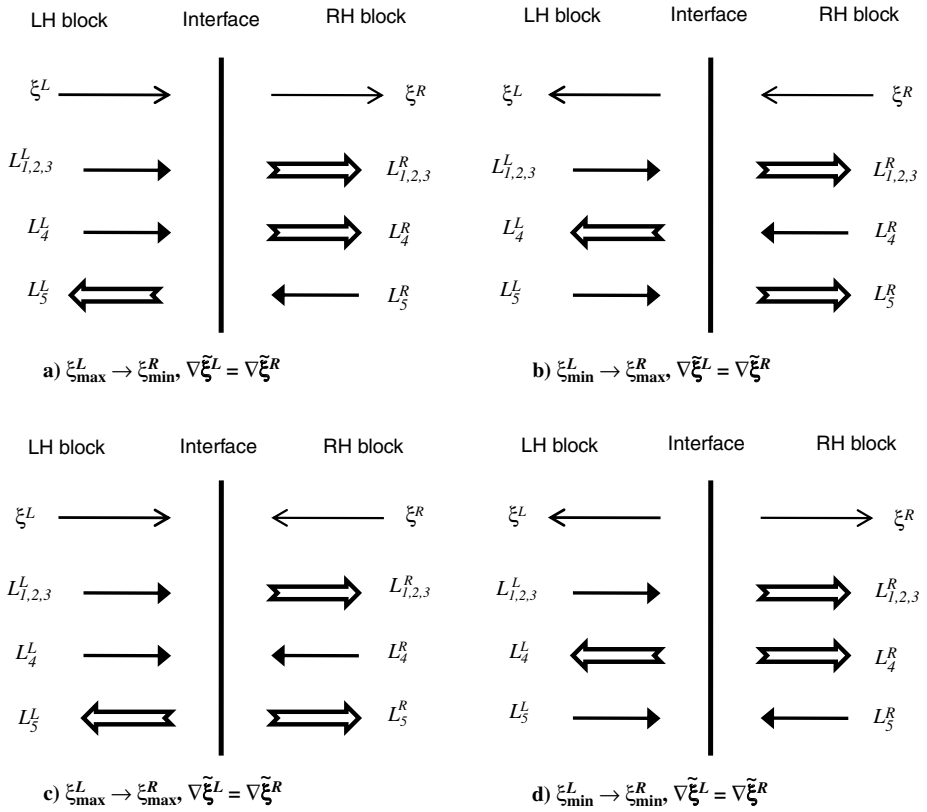

Fig. 1 Summary of the subsonic generalized interface condition showing convection term directions and generalized coordinate alignments where the contravariant velocity U is in the left to right direction.

IV. Patched Characteristic Interface Conditions

The patched grid technique refers to an arbitrary number and distribution of grid points on either side of an interface between two blocks. Thus the grid points on either side of the interface do not generally coincide. There are several problems which make the use of patched grid methods in finite difference codes difficult. These include the treatment of the interior finite differencing stencil that is discontinuous at the patched interface, and communication of the flow variables across the patched interface.

The CICs promote a natural extension to a patched grid technique since it offers a solution to both of these problems. The idea is to decompose the domain along both the patched grid lines just as the CICs decompose the domain along skewed grid lines. Often the patched and skewed interfaces can be made to coincide during grid generation. Thus the interior blocks are decomposed into virtual blocks in that the numerical stencils do not cross and the CICs can be used for the exact interblock communication of the flow variables. The problem remains to approximate the characteristic convection terms at the same point along the interface on either side of the boundary. This can be achieved through a variety of interpolation methods and a proposed method is presented in Sec. V. The patched CICs approach is described by Fig. 2 which shows the decomposition of the blocks into virtual blocks.

The patched CICs have several advantageous properties that leads to a simple implementation, especially in codes where use of characteristic boundary conditions have already been adopted. First, in curvilinear coordinates the block boundaries form a line interface in two-dimensions and a surface interface in three-dimensions. Therefore, two-dimensional and three-dimensional problems require only a one-dimensional and two-dimensional interpolation, respectively, if the interpolation is performed in the computational curvilinear space. In contrast, overset grid methods [3–5] there is no such relationship between grid points and therefore the identification of donor/receiver points and complex hole cutting procedures are required and the degree of interpolation cannot be reduced. Secondly, since no ghost points are required for the proposed method, parallel

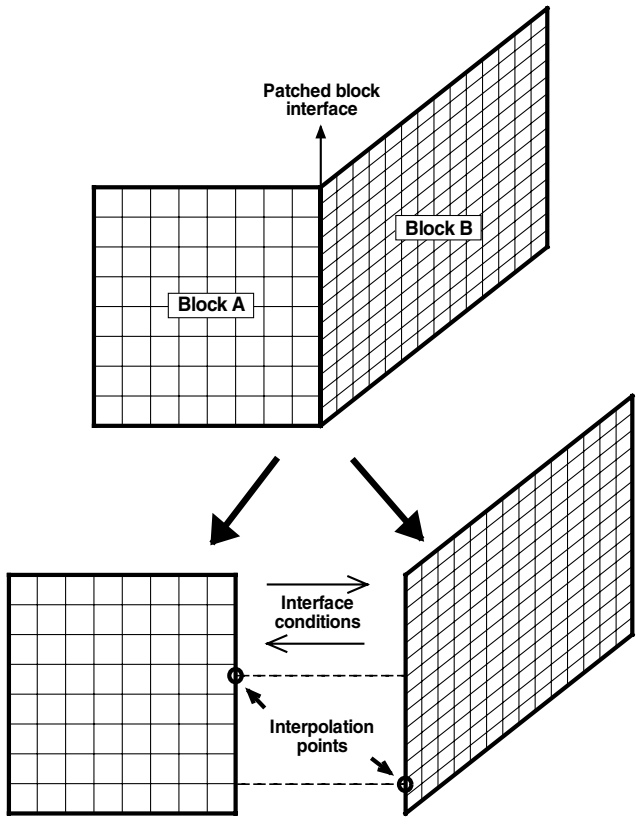

Fig. 2 Decomposition of two blocks joined by a patched interface into virtual blocks.

communication is minimized requiring only transfer of the characteristic convection vector at the boundary nodes $\boldsymbol{L}$ between blocks. In contrast, overset methods require the communication of overlapping arrays of ghost points increasing the level of parallel communication required.

The steps that describe the implementation procedure are as follows:

1) The nearest neighboring grid points along the patched interface are determined using a search algorithm. These are stored for future reference.

2) The interpolation parameters described in Sec. V are computed and used to obtain the interpolation coefficients.

3) The inviscid and viscous flux derivatives in Eq. (1) are calculated independently for each block in the entire domain using a high-order finite differencing scheme. The normal flux derivative $\partial \boldsymbol{E}/\partial \xi$ on the interface is used as an initial guess to be corrected next.

4) The characteristic convection term on each side of the interface, $\boldsymbol{L}$, is calculated using the following identity:

$$\boldsymbol{L} = J\bar{\boldsymbol{P}}^{-1}\left\{\frac{\partial \hat{\boldsymbol{E}}}{\partial \xi} - \left[\boldsymbol{E}\frac{\partial}{\partial \xi}\left(\frac{\xi_x}{J}\right) + \boldsymbol{F}\frac{\partial}{\partial \xi}\left(\frac{\xi_y}{J}\right) + \boldsymbol{G}\frac{\partial}{\partial \xi}\left(\frac{\xi_z}{J}\right)\right]\right\} \tag{22}$$

5) High-order interpolation is performed to obtain the characteristic convection terms $\boldsymbol{L}^L$ and $\boldsymbol{L}^R$ corresponding to the same location along the interface.

6) The generalized interface conditions are imposed to correct the characteristic convection term. The new corrected characteristic convection term is represented by $\boldsymbol{L}^*$.

7) The normal-flux derivative term is then recalculated by the corrected characteristic convection term using the following identity:

$$\left(\frac{\partial \hat{\boldsymbol{E}}}{\partial \xi}\right)^* = \frac{1}{J}\bar{\boldsymbol{P}}\boldsymbol{L}^* + \left[\boldsymbol{E}\frac{\partial}{\partial \xi}\left(\frac{\xi_x}{J}\right) + \boldsymbol{F}\frac{\partial}{\partial \xi}\left(\frac{\xi_y}{J}\right) + \boldsymbol{G}\frac{\partial}{\partial \xi}\left(\frac{\xi_z}{J}\right)\right] \tag{23}$$

This new corrected term is then returned to Eq. (1) to be integrated in time.

Steps 1 and 2 are only performed once during the solution initialization, whereas steps 3–7 are repeated for each block in the domain at each stage of the time-stepping cycle to update the solution accordingly. At coincident points where no interpolation is required the primitive variables are matched at the end of each time step so that differences due to round-off errors are removed [7].

V. Numerical Algorithms

A. Spatial and Time Discretization

High-order FDSs are employed to approximate the inviscid and viscous flux derivatives and metric terms. The schemes should have low dispersion and dissipation errors that are required to solve CAA problems. Particular attention should be paid to the boundary schemes since they are relied upon to preserve accuracy at the interior interfaces.

The fourth-order optimized prefactored compact scheme of Ashcroft and Zhang [13] is employed in the current work. The optimization procedure based on Fourier analysis was used to determine the coefficients of the biased stencils. The optimization strategy sacrifices the schemes formal order of accuracy in favor of enhanced resolution characteristics across the range of wave numbers realizable on a given mesh. The optimized prefactored compact schemes have smaller stencil sizes and require only the solution of two independent bidiagonal matrices.

The prefactorization strategy splits the central implicit schemes into forward and backward biased operators. The forward and backward operators D_i^F and D_i^B at grid point, i, are derived such that

$$D_i = \frac{1}{2}(D_i^F + D_i^B) \tag{24}$$

The forward and backward operators for the fourth-order five-point scheme used for interior grid points are given as follows:

$$\frac{1}{2}D_i^F = \frac{1}{2\beta_F \Delta\xi}[b_F(f_{i+1} - f_i) + d_F(f_{i-1} - f_i) + e_F(f_{i-2} - f_i)] - \frac{\alpha_F}{2\beta_F}D_{i+1}^F \tag{25}$$

$$\frac{1}{2}D_i^B = \frac{1}{2\beta_F \Delta\xi}[b_F(f_i - f_{i-1}) + d_F(f_i - f_{i+1}) + e_F(f_i - f_{i+2})] - \frac{\gamma_B}{2\beta_B}D_{i-1}^B \tag{26}$$

where the coefficients α, β, γ, b, d, e are given by Ashcroft and Zhang [13], f_i denotes the value of the function f at grid point i, and $\Delta\xi$ is the uniform spacing along a given coordinate direction in computational space. Additional boundary stencils are required at grid points $i = 1, 2$ and $i = N - 1, N$. For these points a third-order boundary formulation is used where the explicit backward and forward stencils are given by

$$D_2^B = \frac{1}{\Delta\xi}\sum_{i=1}^{4} s_i f_i, \qquad D_{N-1}^B = \frac{1}{\Delta\xi}\sum_{i=N-3}^{N} e_i f_i \tag{27}$$

$$D_2^F = \frac{1}{\Delta\xi}\sum_{i=1}^{4} -e_{N+1-i} f_i, \qquad D_{N-1}^F = \frac{1}{\Delta\xi}\sum_{i=N-3}^{N} -s_{N+1-i} f_i \tag{28}$$

where the coefficients s_i $(i = 1, \ldots, 4)$ and e_i $(i = N - 3, \ldots, N)$ are given by Ashcroft and Zhang [13]. At the actual boundary points $i = 1$ and $i = N$ the following one-sided third-order explicit stencil is used:

$$D_1 = \frac{1}{\Delta\xi}\sum_{i=1}^{4} c_i f_i, \qquad D_N = \frac{1}{\Delta\xi}\sum_{i=N-3}^{N} -c_{N+1-i} f_i \tag{29}$$

where $c_1 = 33/18$, $c_2 = 3$, $c_3 = -3/2$ and $c_4 = 1/3$. The error of the overall scheme has been shown to decay in accordance of the idealized (fourth-order) convergence rate indicating that the third-order boundary closures are sufficient to ensure fourth-order global accuracy [13,14].

Although the high-order FDSs are able to resolve a wider range of wave numbers than low-order schemes they do not resolve the highest wave numbers effectively. Therefore a sixth-order explicit filter was adopted to filter the conserved variables in each coordinate direction in order to remove any unwanted numerical oscillations in the unresolved range. The filtering is performed at the end of each time step.

Temporal integration was performed using the 4–6 low dispersion and dissipation Runge–Kutta optimized scheme of Hu et al. [15]. It is a two-step alternating scheme in which different coefficients are employed in the alternating steps. The low storage implementation of this scheme was employed in this work. When combined with the spatial scheme the stable CFL limit of the temporal integration is 1.011.

B. High-Order Interpolation

High-order interpolation is required to approximate the characteristic convection term, $\boldsymbol{L}$, at the unknown point on the adjacent block. It is important that the interpolation error of a particular scheme is minimized and that the accuracy of the spatial scheme is maintained. Lagrangian polynomial interpolation has been a popular choice in high-order overset grid methods for CAA applications [4,5]. The error of an interpolation scheme is usually indicated by the Taylor series truncation term, whereas a more quantitative measure of error is preferable in CAA applications. In response, Tam and Kurbatskii [16] developed a one-dimensional optimized interpolation method based upon wave number analysis so that the interpolation error could be quantified. Sherer and Scott [17]

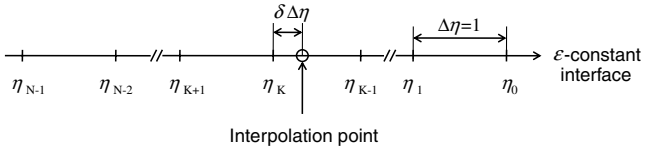

Fig. 3 Definition of *N*-point interpolation stencil along one-dimensional ξ constant interface.

compared the optimized interpolation method of Tam and Kurbatskii with the B-Spline method. Their error analysis indicated that the optimized method is far superior.

For the two-dimensional test cases presented in this paper the one-dimensional optimized method [16] of various orders is compared with Lagrangian polynomial interpolation. Consider the one-dimensional interpolation stencil represented along a ξ-constant interface formed by N uniformly spaced donor points and $K = N - 1$ subintervals with an arbitrarily located interpolation point as shown in Fig. 3. The stencil points correspond to the grid points along the patched interface of one block, and the interpolation point corresponds to a point belonging to the adjacent block. By specifying that the interpolation is performed in computational space the uniform interval width of $\Delta\eta = 1$ is justified.

The approximation of the characteristic convection term located arbitrarily within the Kth stencil interval to the right of η_K can be expressed as

$$L_m(\eta_0 - (K-\delta)\Delta\eta) = \sum_{j=0}^{N-1} S_j L_{m_j}, \qquad m = 1, 2, \ldots, 5 \tag{30}$$

where L_{m_j} is the value of the characteristic convection term at stencil point j, m are components of the vector, S_j are the interpolation coefficients, and $\delta\Delta\eta$ is the offset of the interpolation point measured to the right of η_K. In the case of Lagrangian polynomial interpolation S_j is replaced by the Lagrange polynomial coefficients formed by the N stencil points, which are given by

$$\ell_k^{(N)}(\eta) = \prod_{j=0, j\neq k}^{N-1} \frac{(\eta_0 - (K-\delta)\Delta\eta - \eta_j)}{(\eta_k - \eta_j)}$$
$$k = 0, 1, 2 \ldots, (N-1) \tag{31}$$

For the optimized interpolation scheme Tam and Kurbatskii [16] defined the local error as

$$\bar{E}_{\text{local}} = \left| e^{-i(K-\delta)\alpha\Delta\eta} - \sum_{j=0}^{N-1} S_j e^{-ij\alpha\Delta\eta} \right|^2 \tag{32}$$

where α is the wave number. Following their wave number analysis the optimized interpolation coefficients, S_j, are given by the solution to the following algebraic equations:

$$\sum_{j=0}^{N-1} S_j \frac{\sin(\ell - j)\kappa}{(\ell - j)} + \frac{\lambda}{2} = \frac{\sin(\ell - K + \delta)\kappa}{(\ell - K + \delta)}$$
$$\ell = 0, 1, 2 \ldots, (N-1) \tag{33}$$

$$\sum_{j=0}^{N-1} S_j = 1 \tag{34}$$

Equations (33) and (34) can be solved simultaneously using Gaussian elimination to yield the interpolation coefficients. The suggested value of 1.0 for the interpolation parameter κ was adopted in all computations. The extension of the one-dimensional interpolation methods to two-dimensions (required for three-dimensional computations) is done by lines with the interpolation broken down into a number of one-dimensional problems [18].

VI. Results

A. Vortex Convection

The performance of the patched CICs is first evaluated by solving the problem of vortex convection in an otherwise uniform inviscid subsonic flow [19]. The Euler equations are solved in curvilinear coordinates. The vortex is prescribed by the following relations:

$$u = M_\infty - \frac{C(y - y_c)}{R^2}\exp(-r^2/2), \qquad v = \frac{C(x - x_c)}{R^2}\exp(-r^2/2)$$
$$p' = p_\infty - p = \frac{\rho C^2}{2R^2}\exp(-r^2) \qquad r^2 = \frac{(x - x_c)^2 + (y - y_c)^2}{R^2}$$
$$\rho' = p'$$

where x_c and y_c define the coordinates of the vortex center at $t = 0$, $R = 1.0$ is the vortex core radius. The nondimensional vortex strength parameter $C/U_\infty R$ was set to 0.02 and the freestream Mach number was set to $M_\infty = 0.1$. In the calculation the length scales are nondimensionalized by $L^* = 1$ m, the velocities by $c_\infty = 340$ m/s, the density by $\rho_\infty = 1.225$ kg/m^3 and the pressure by $\rho_\infty c_\infty^2$.

The computational grid of dimensions $-8 \le x \le 8$; $-8 \le y \le 8$ consists of three blocks shown in Fig. 4a. Blocks 1 and 3 are of the same resolution whereas block two is of a higher resolution so that a patched interface is formed between the blocks. The patching ratio is defined as the ratio of the grid points along the interface of block 1 to that of block 2. Periodic boundary conditions are prescribed along each exterior boundary so that the vortex convecting along the line $y = 0$ leaves block 3 and reappears in block 1. Communication

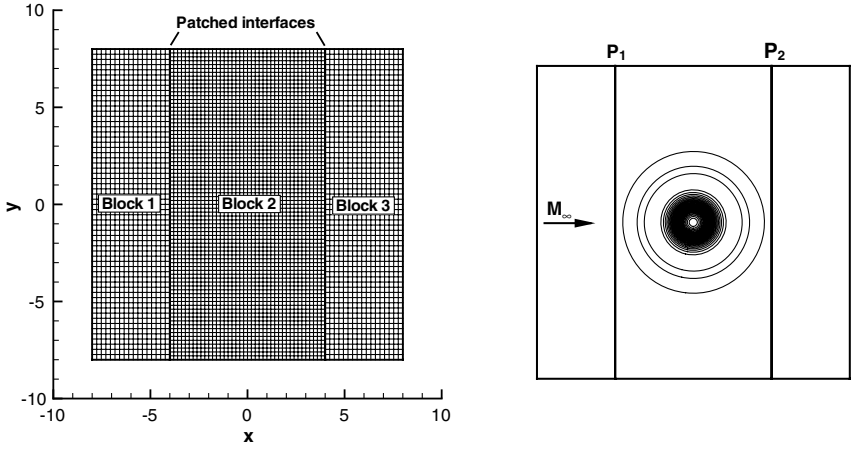

a) b)

Fig. 4 Vortex convection validation case: a) three-block grid with patched interfaces P1 and P2 defined along the block interfaces and b) contours of vorticity magnitude after $t = 16$.

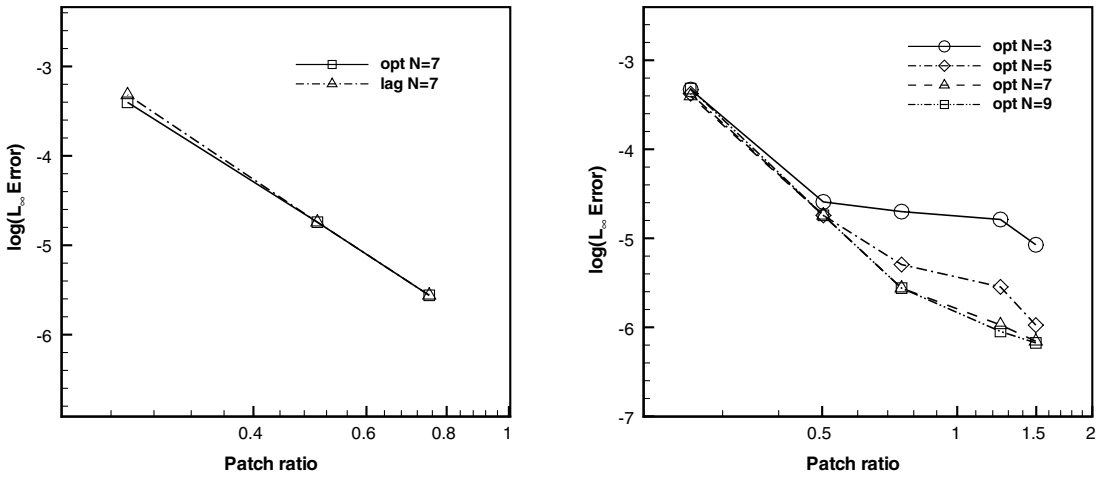

a) b)

Fig. 5 Influence of patching ratio on solution error for the test case of inviscid vortex convection: a) swirl velocity error for optimized seven-point stencil (opt $N = 7$) and seven-point Lagrangian polynomial (lag $N = 7$) interpolation and b) comparison of optimized method for stencil size $N = 3, 5, 7, 9$.

between the periodic boundaries is performed using the CICs. At time $t = 0$ the vortex is centered at (0,0) and at $t = 16$ the vortex returns to its original position having convected through both block boundaries as shown in Fig. 4b. A low CFL of approximately 0.5 is adopted in each simulation so that time-stepping error is minimized. High-order explicit filtering is applied which had negligible effect on the measured quantities except to suppress spurious grid and interpolation oscillations especially in the case of the coarser grids and higher patching ratios.

1. Influence of Patching Ratio and Interpolation Method

Computations are performed at patching ratios between 0.25 and 0.75 by maintaining a resolution of 81×161 for block 2 and varying the density of blocks 1 and 3. The Lagrange polynomial and optimized interpolation methods are compared each maintaining a seven-point stencil. The maximum error (L_∞) in the computed vertical velocity component along $y = 0$ at the end of the simulation is used to measure the accuracy of the computations. The results obtained using interpolation methods with $N = 7$ point stencils are shown in Fig. 5a. It is clear that the error increases as the patching ratio decreases due to a combination of grid coarsening and disparate interpolation stencil widths on each sides of the interface. The difference between the two interpolation methods is shown to be small [16] reaching a maximum at the smallest patching ratio.

2. Influence of Patching Ratio and Interpolation Stencil Point Number

The problem is solved using optimized interpolation for various N stencil points to assess the effect of the number of stencil points, N, on the solution error. In a practical problem the number of stencil points should be high enough to minimize interpolation error and it is desirable that the global accuracy is be degraded by the interpolation. For a comprehensive comparison, interpolation schemes with $N = 3$, 5, 7, 9 stencil points are investigated. Once more the resolution of block 2 is maintained while blocks 1 and 3 are gradually refined to achieve patch ratios between 0.25–1.5. Results for a patching ratio of 1 are omitted since in this case the interpolation scheme becomes redundant and the results are plotted in Fig. 5b. The results show that the error reduces as the patch ratio and therefore global grid resolution both increase. The result also shows that in the case that the patch ratio is very small and the grid on one side of the interface is very coarse, grid quality dominates the solution error which also becomes less sensitive to N. Conversely, as the patch ratio increases and the grid is refined then the error becomes more sensitive to N. The error continues to reduce as the patch ratio increases above 1

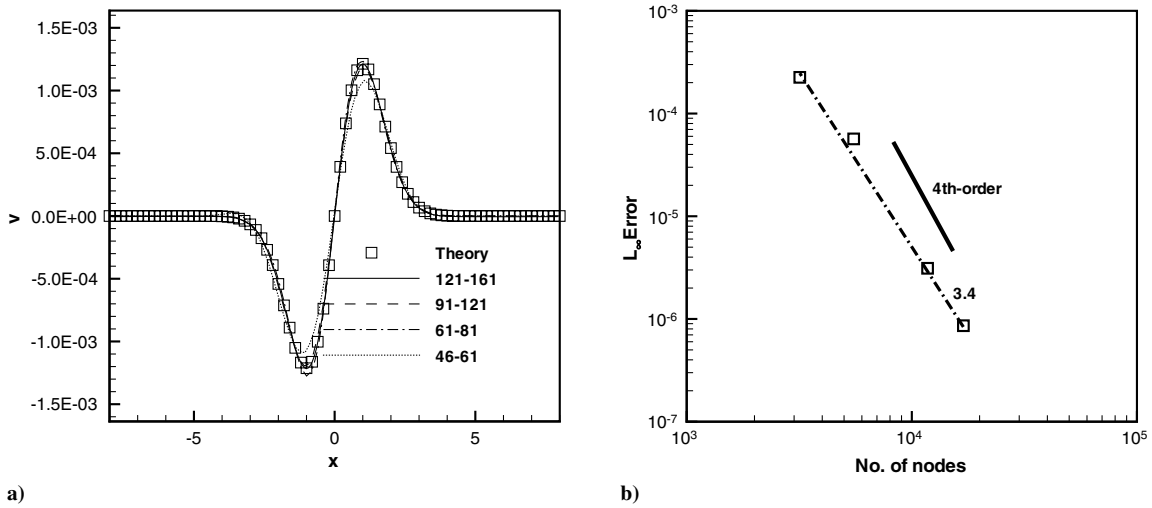

a) b)

Fig. 6 Vortex test case grid convergence: a) swirl velocity prediction along $y = 0$ for various grid resolutions where #-# designates the number of nodes along the interface of blocks 1 and 2, respectively and b) convergence rate of patched CICs with seven-point optimized interpolation method combined with the fourth-order spatial discretization scheme (third-order boundary formulation) of Ashcroft and Zhang [13].

indicating that the solution is more sensitive to the overall grid quality than the patch ratio. The results show that in this case a seven-point interpolation stencil is adequate to minimize interpolation error.

3. Grid Convergence Study

It has previously been shown that the error of the interior and boundary formulations of the spatial scheme decays in accordance to the idealized (fourth-order) convergence rate [13]. It is therefore important to assess whether the addition of an interpolation scheme would affect the realizable order of accuracy. The actual order of the patched CICs is assessed running the test case at various grid resolutions and plotting the $\log(L_\infty)$ error vs number of grid nodes. In each case the block sizes are scaled proportionally to obtain coarser/finer grids while keeping the patching ratio of 0.75 constant. The seven-point optimized interpolation method is adopted in this test. The results of the test are shown in Figs. 6a and 6b where #-# designates the number of nodes along the interface of blocks 1 and 2, respectively. A least squares fit of the data is performed and reveals an order of accuracy for this test case of 3.4, falling between the accuracy of the boundary scheme and the interior scheme.

B. Gaussian Pulse Propagation

Next the benchmark problem of the free-field acoustic propagation and convection of an initial pulse through skewed and patched blocked boundaries is considered. The initial condition at time $t = 0$ is given by

$$p'(x, y, 0) = \epsilon \exp\left[-\ell_n 2\left(\frac{(x+10)^2 + (y)^2}{9}\right)\right], \qquad (35)$$
$$u'(x, y, 0) = 0, \qquad v'(x, y, 0) = 0, \qquad \rho' = p'$$

where x and y are the Cartesian coordinates; t is time; u' and v' are velocity perturbations in the x and y directions respectively; and p' is the pressure perturbation. A freestream Mach number of $M = 0.5$ is

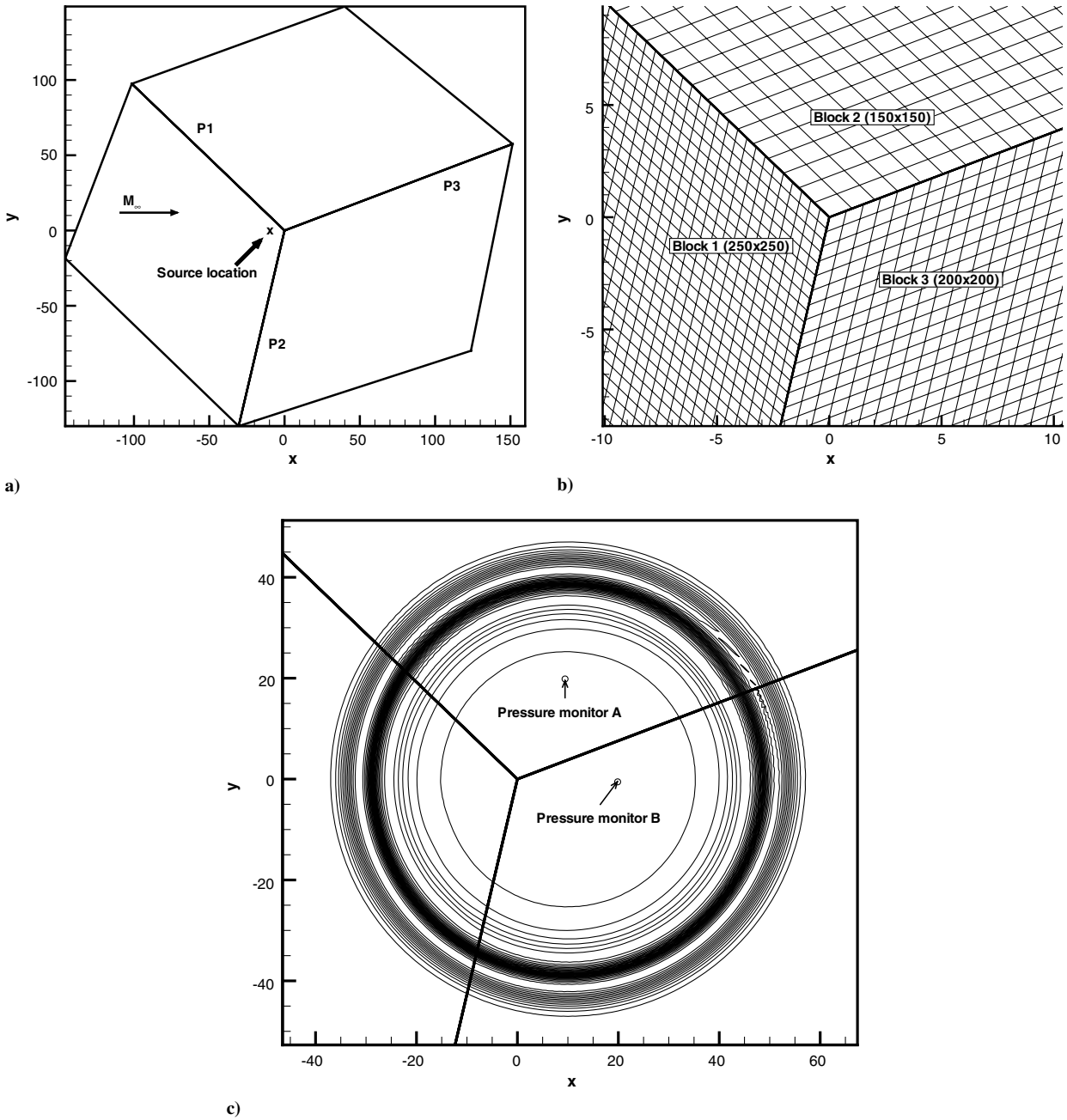

Fig. 7 Gaussian pulse propagation across highly skewed block boundaries: a) domain description and initial pressure pulse location, b) patching of blocks in vicinity of multiblock junction, and c) pressure perturbation field after $t = 40$.

specified and a small initial pulse amplitude of $\epsilon = 10^{-4}$ was set so that the solution of the linearized Euler equations can be accurately approximated by the computed solution of the Euler equations. In the calculation the length scales are nondimensionalized by $L^* = 1$ m, the velocities by $c_\infty = 340$ m/s, the density by $\rho_\infty = 1.225$ kg/m^3 and the pressure by $\rho_\infty c_\infty^2$.

To test the versatility of the patched interface conditions a highly skewed three-block grid is generated as shown in Fig. 7. In this case the generalized CICs presented in Sec. III are required due to the relative metric alignments between the blocks. The grid consists of three patching interfaces P1, P2, and P3, with patching ratios of 0.6, 0.8 and 0.75, respectively. Along the exterior boundaries a nonreflecting buffer zone boundary condition [20] was imposed. A constant CFL of 0.5 was adopted in each computation. The pulse was initiated at $(-10, 0)$ and the pressure field was obtained at $t = 40$ as shown in Fig. 7c.

An exact solution has been obtained for this problem [21] and the computed pressure history was obtained at points A and B located at (8.9,19.8) and (28.5,0.0), respectively. Results for computations using the optimized $N = 7$ point interpolation scheme are presented in Fig. 8. Results from interpolation schemes of $N = 3$–9 stencil points were compared and the solution was shown to be insensitive to $N > 5$. It is clear that the pulse radiates and convects correctly through the patched block interfaces and that the differences between the exact and computed solutions are small at both monitor locations. The computation was run until the pulse had propagated through the entire domain and no adverse effects such as reflections due to the patched interfaces were observed.

C. Cylinder Scattering

Finally, the two-dimensional scattering problem from the Second CAA Workshop on Benchmark problems [22] is considered. The physical problem is to find the sound field generated by a propeller scattered off by the fuselage of an aircraft. The fuselage is idealized as a circular cylinder of radius $R = 0.5$ located at the origin and the noise source as line source so that the computational problem is two-dimensional. At time $t = 0$, the initial conditions are given by

$$p'(x, y, 0) = \epsilon \exp\left[-\ell n\, 2\left(\frac{(x-4)^2 + (y)^2}{0.04}\right)\right], \qquad u'(x, y, 0) = 0, \qquad v'(x, y, 0) = 0, \qquad \rho' = p' \tag{36}$$

The problem asks for the pressure time history at three locations corresponding to the Cartesian coordinates (0,5), $(-3.54, 3.54)$ and $(-5, 0)$ between time $t = 6 \rightarrow 10$. The value of initial pulse amplitude is set to $\epsilon = 10^{-4}$ so that the solution of the linearized Euler equations can be accurately approximated by the computed solution of the Euler equations. The exact solution [22] has been found at the three locations. Again, length scales are nondimensionalized by $L^* = 1$ m, the velocities by $c_\infty = 340$ m/s, the density by $\rho_\infty = 1.225$ kg/m^3 and the pressure by $\rho_\infty c_\infty^2$.

The computational domain is circular extending radially from $R = 0.5$ to $R = 18$ and is decomposed into three blocks as shown in Fig. 9. Patched interfaces are defined along the block boundaries by specifying block dimensions of 61×161, 81×241 and 61×401 for blocks 1–3, respectively. The resulting patching ratios of the patched interfaces P1 and P2 formed between blocks 1–2 and 2–3, are $2/3$ and $3/4$ respectively. The patching allowed the desired grid spacing to be maintained in the cylinder far-field without leading to unnecessarily small cell sizes close to the cylinder. This problem is also a stringent test for curved wall boundary conditions and the characteristic wall boundary conditions proposed by Kim and Lee [23] are adopted in this test. A nonreflecting buffer zone boundary condition [20] was imposed along the external boundaries. A CFL of 0.5 is employed in all simulations along with the optimized seven-point interpolation method.

Figure 10 shows the computed pressure contours at $t = 1.5$, 4.0 and 7.0. At $t = 1.5$ the initial pulse is clearly seen before interaction with the cylinder wall. At $t = 4.0$ the interaction of the pulse and solid wall is clearly seen resulting in the scattered pressure field shown at $t = 7.0$. The pressure disturbance appears to propagate through the patched interfaces accurately. Figure 11 provides a more comprehensive comparison by comparing the time history at the three specified locations with the exact solution. The result shows that the differences between the exact result and the computation are small at all locations. The error using interpolation schemes of $N = 3$, 5, 7, and 9 stencil points was quantified in terms of the maximum percentage error in the computed perturbed pressure monitored at observer $(-5, 0)$. The maximum percentage error for the $N = 3$ point optimized interpolation scheme as 7.8%, whereas

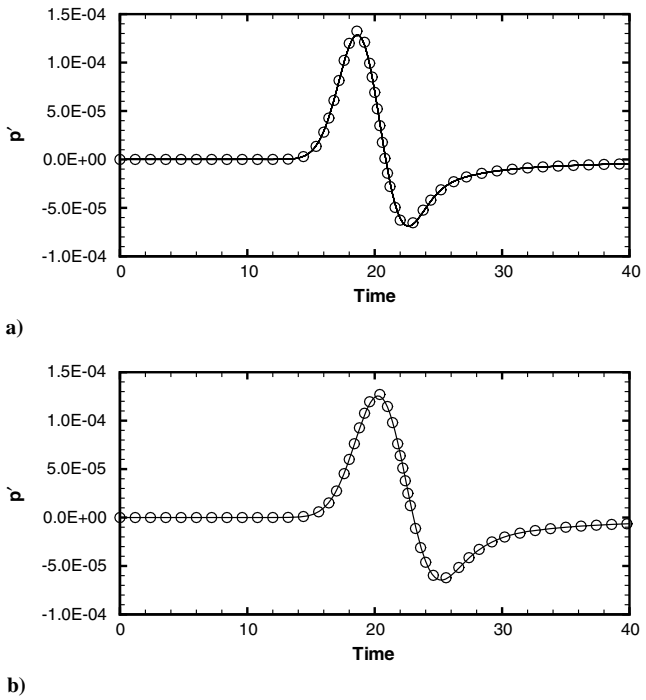

Fig. 8 Acoustic pressure pulse propagation and convection across highly skewed block boundaries: a) pressure time history of acoustic pressure pulse propagation and convection after time $t = 40$ at monitor A located at (8.9,19.8) and b) at monitor B located at (28.5,0.0). (—) Patched CICs computation, (\circ) exact solution.

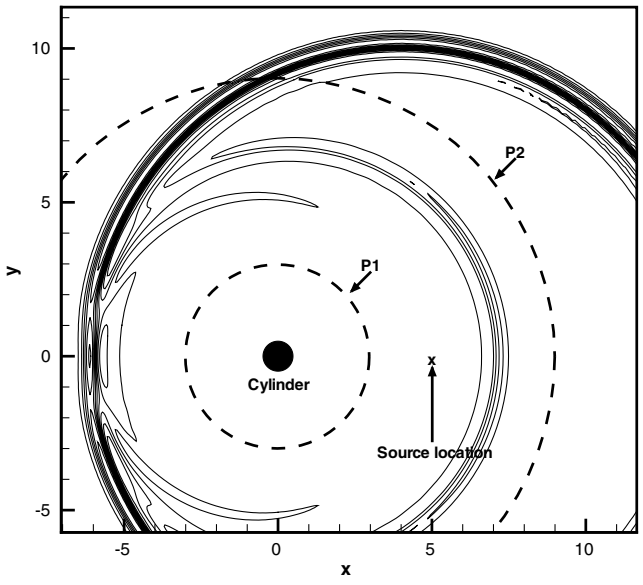

Fig. 9 Two-dimensional scattering problem setup showing patched interfaces P1 and P2 (dashed lines), source location at $t = 0$, and computed pressure contours at $t = 10$.

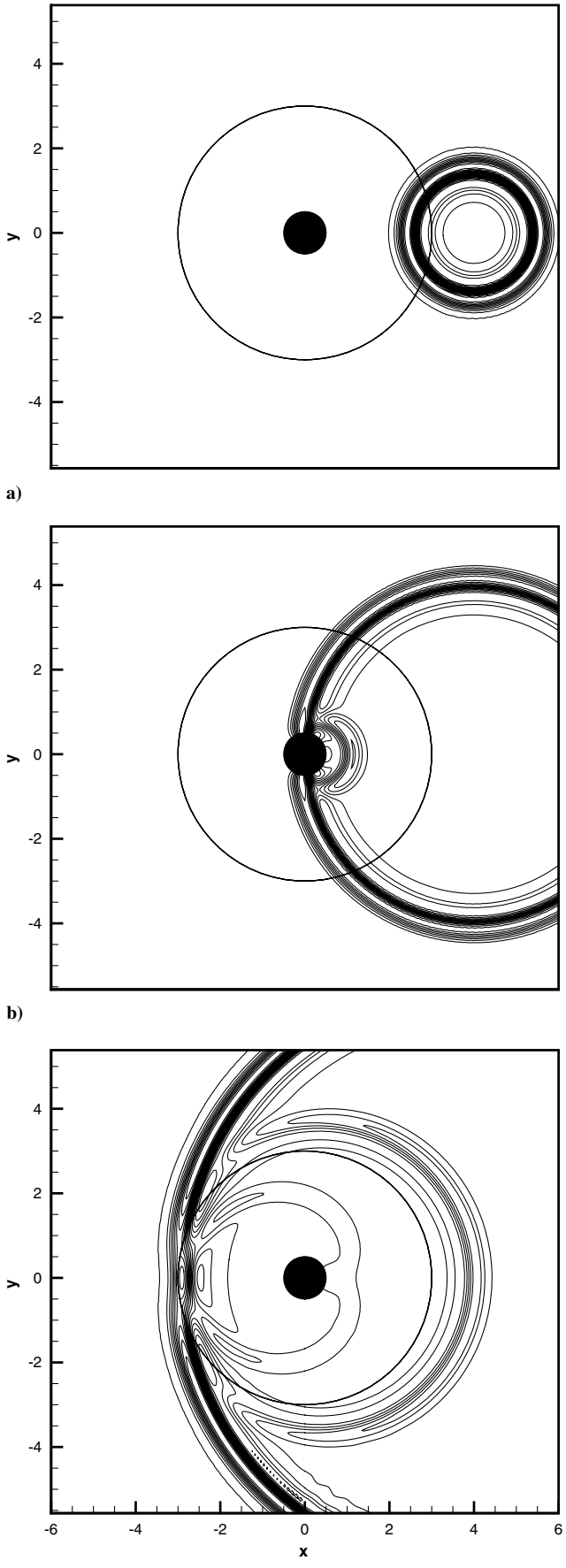

Fig. 10 Pressure contours showing the scattering of an acoustic pulse by a solid circular cylinder at: a) $t = 1.5$, b) $t = 4.0$, and c) $t = 7.0$. Solid cylinder represented by solid black circle, patch interface P1 shown by circular line at $R = 3.0$.

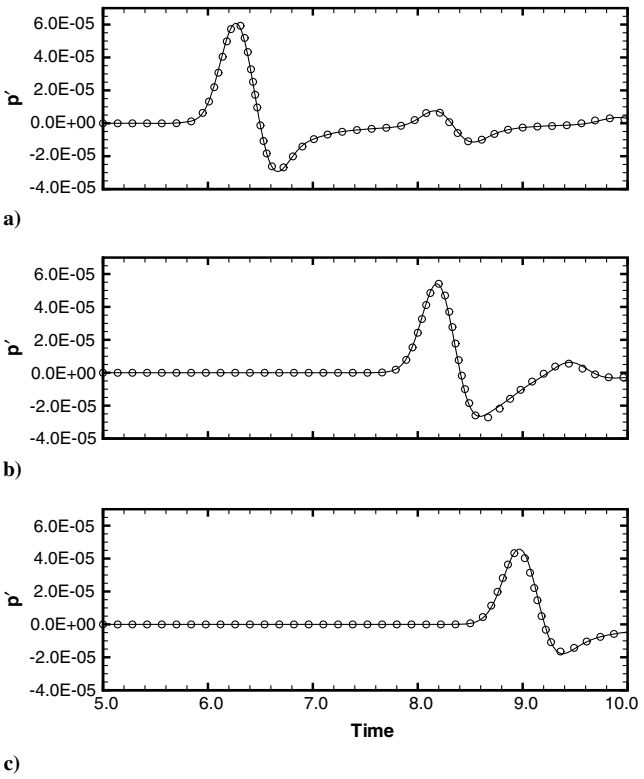

Fig. 11 Comparison between computed and exact solutions of two-dimensional scattering problem: a) pressure time history at (0,5), b) pressure time history at (−3.54, 3.54), and c) pressure time history at (−5, 0). (—) Patched CICs computation, (\circ) exact solution.

the error converged for $N > 3$ schemes with maximum percentage errors in the range of 5.3% ±0.1%.

VII. Conclusions

Patched CICs have been proposed for high-order aeroacoustic computation. The patched CICs extend the original CICs by allowing nonmatching grid points to be arbitrarily distributed along the interface. The computational domain is decomposed along patched and skewed grid lines, leaving the blocks disconnected, and the CICs are used to recover interblock communication. A simple way of deriving the generalized CICs has also been presented. High-order optimized interpolation was proposed to approximate the characteristic convection term at the same position on either side of the interface. Various benchmark problems were used to validate the patched CICs and investigate the effect of various parameters on the solution error. The results show that the accuracy of the spatial schemes can be maintained if an appropriate number of stencil points is chosen for the interpolation. It has also been shown that the patching ratio is a key parameter and that care should be taken to ensure that the resolution characteristics on either side of the interface are suitable. The relationship between patching ratio and the number of interpolation stencil points has been investigated. It was shown that in the case that there is a high degree of patching and the grid on one side of the interface becomes too coarse, grid quality dominates the solution error which becomes less sensitive to the number of stencil points. Conversely, as the grid is refined the solution error can be reduced by increasing the size of the interpolation stencil.

Appendix: Characteristic Transformation Matrices

The matrix $\bar{\boldsymbol{P}}^{-1}$ transforms the conservative variables to characteristic variables. $\bar{\boldsymbol{P}}^{-1}$ and its inverse $\bar{\boldsymbol{P}}$ diagonalize the flux-Jacobian matrices in the direction normal to the interface. These transformation matrices are given as

$$\bar{\boldsymbol{P}}^{-1} = \begin{bmatrix} \boldsymbol{B_o}\cdot\boldsymbol{l}_x & (\gamma-1)\frac{u}{c^2}\tilde{\xi}_x & (\gamma-1)\frac{v}{c^2}\tilde{\xi}_x+\frac{\tilde{\xi}_z}{\rho} & (\gamma-1)\frac{w}{c^2}\tilde{\xi}_x-\frac{\tilde{\xi}_y}{\rho} & -\frac{\gamma-1}{c^2}\tilde{\xi}_x \\ \boldsymbol{B_o}\cdot\boldsymbol{l}_y & (\gamma-1)\frac{u}{c^2}\tilde{\xi}_y-\frac{\tilde{\xi}_z}{\rho} & (\gamma-1)\frac{v}{c^2}\tilde{\xi}_y & (\gamma-1)\frac{w}{c^2}\tilde{\xi}_y-\frac{\tilde{\xi}_x}{\rho} & \frac{\gamma-1}{c^2}\tilde{\xi}_y \\ \boldsymbol{B_o}\cdot\boldsymbol{l}_z & (\gamma-1)\frac{u}{c^2}\tilde{\xi}_z+\frac{\tilde{\xi}_y}{\rho} & (\gamma-1)\frac{v}{c^2}\tilde{\xi}_z-\frac{\tilde{\xi}_x}{\rho} & (\gamma-1)\frac{w}{c^2}\tilde{\xi}_z & \frac{\gamma-1}{c^2}\tilde{\xi}_y \\ \frac{c}{\rho}\left(\frac{\gamma-1}{2}M^2-\frac{\boldsymbol{v}\cdot\boldsymbol{l}_\xi}{c}\right) & \boldsymbol{C}_+\cdot\boldsymbol{l}_x & \boldsymbol{C}_+\cdot\boldsymbol{l}_y & \boldsymbol{C}_+\cdot\boldsymbol{l}_z & \frac{\gamma-1}{\rho c} \\ \frac{c}{\rho}\left(\frac{\gamma-1}{2}M^2-\frac{\boldsymbol{v}\cdot\boldsymbol{l}_\xi}{c}\right) & \boldsymbol{C}_-\cdot\boldsymbol{l}_x & \boldsymbol{C}_-\cdot\boldsymbol{l}_y & \boldsymbol{C}_-\cdot\boldsymbol{l}_z & \frac{\gamma-1}{\rho c} \end{bmatrix}$$

$$\bar{\boldsymbol{P}} = \begin{bmatrix} \tilde{\xi}_x & \tilde{\xi}_y & \tilde{\xi}_z & \frac{\rho}{2c} & \frac{\rho}{2c} \\ u\tilde{\xi}_x & u\tilde{\xi}_y-\rho\tilde{\xi}_z & u\tilde{\xi}_z+\rho\tilde{\xi}_y & \frac{\rho}{2c}(u+\tilde{\xi}_x c) & \frac{\rho}{2c}(u+\tilde{\xi}_x c) \\ v\tilde{\xi}_x+\rho\tilde{\xi}_z & v\tilde{\xi}_y & v\tilde{\xi}_z-\rho\tilde{\xi}_x & \frac{\rho}{2c}(v+\tilde{\xi}_y c) & \frac{\rho}{2c}(v+\tilde{\xi}_y c) \\ w\tilde{\xi}_x+\rho\tilde{\xi}_y & w\tilde{\xi}_y+\rho\tilde{\xi}_x & w\tilde{\xi}_z & \frac{\rho}{2c}(w+\tilde{\xi}_z c) & \frac{\rho}{2c}(w+\tilde{\xi}_z c) \\ \boldsymbol{b}\cdot\boldsymbol{l}_x & \boldsymbol{b}\cdot\boldsymbol{l}_y & \boldsymbol{b}\cdot\boldsymbol{l}_z & \frac{\rho}{2c}(\boldsymbol{H}+c\boldsymbol{v}\cdot\boldsymbol{l}_\xi) & \frac{\rho}{2c}(\boldsymbol{H}-c\boldsymbol{v}\cdot\boldsymbol{l}_\xi) \end{bmatrix}$$

The vectors in $\bar{\boldsymbol{P}}^{-1}$ and $\bar{\boldsymbol{P}}$ are defined as follows:

$$\boldsymbol{B}_o = \left(1-\frac{\gamma-1}{2}M^2\right)\boldsymbol{l}_x - \frac{1}{\rho}(\boldsymbol{v}\times\boldsymbol{l}_\xi), \qquad \boldsymbol{C}_\pm = \pm\frac{\boldsymbol{l}_\xi}{\rho} - \frac{\gamma-1}{\rho c}\boldsymbol{v},$$

$$\boldsymbol{v} = (u, v, w)^T \qquad \boldsymbol{b} = \frac{|\boldsymbol{v}|^2}{2}\boldsymbol{l}_\xi + \rho(\boldsymbol{v}\times\boldsymbol{l}_\xi), \qquad \boldsymbol{H} = \frac{|\boldsymbol{v}|^2}{2} + \frac{c^2}{\gamma-1}$$

where $\boldsymbol{l}_x$, $\boldsymbol{l}_y$, and $\boldsymbol{l}_z$ are unit vectors in the x, y, and z directions, respectively, and

$$\boldsymbol{l}_\xi = \nabla\boldsymbol{\xi}/|\nabla\boldsymbol{\xi}|$$

References

[1] Tam, C. K. W., "Computational Aeroacoustics: Issues and Methods," *AIAA Journal*, Vol. 33, No. 10, 1995, pp. 1788–1796. doi:10.2514/3.12728

[2] Ffowcs Williams, J. E., and Hawkings, D. L., "Sound Generation by Turbulence Surfaces in Arbitrary Motion," *Philosophical Transactions of the Royal Society of London, Series A: Mathematical and Physical Sciences*, Vol. 264, No. 1151, 1969, pp. 321–342.

[3] Delfs, J. W., "An Overlapped Grid Technique for High Resolution CAA Schemes for Complex Geometries," AIAA Paper 2001-2199, 2001.

[4] Sherer, S. E., and Scott, J. N., "Development and Validation of a High-Order Overset Grid Flow Solver," AIAA Paper 2002-2733, 2003.

[5] Sherer, S. E., and Visbal, M. R., "Computational Study of Acoustic Scattering from Multiple Bodies Using a High-Order Overset Grid Approach," AIAA Paper 2003-3203, 2003.

[6] Carpenter, M. H., Nordström, J., and Gottlieb, D., "A Stable and Conservative Interface Treatment of Arbitrary Spatial Accuracy," *Journal of Computational Physics*, Vol. 148, No. 2, 1999, pp. 341–365.

[7] Kim, J. W., and Lee, D. J., "Characteristic Interface Conditions for Multiblock High-Order Computation on Singular Structured Grid," *AIAA Journal*, Vol. 41, No. 12, 2003, pp. 2341–2348. doi:10.2514/2.6858

[8] Sumi, T., Kurotaki, T., and Hiyama, J., "Generalized Characteristic Interface Conditions for High-Order Multi-Block Computation," *International Journal of Computational Fluid Dynamics*, Vol. 21, Nos. 9-10, 2007, pp. 335–350. doi:10.1080/10618560701721736

[9] Sumi, T., Kurotaki, T., and Hiyama, J., "Generalized Characteristic Interface Conditions with High-Order Interpolation Method," AIAA Paper 2008-752, 2008.

[10] Anderson, D. A., Tannehill, J. C., and Pletcher, R. H., *Computational Fluid Dynamics and Heat Transfer*, 2nd ed., Taylor and Francis, Washington, D.C., 1997, pp. 679–714.

[11] Warming, R. F., Beam, R. M., and Hyett, B. J., "Diagonalization and Simultaneous Symmetrization of Gas-Dynamic Matrices," *Mathematics of Computation*, Vol. 29, No. 132, 1975, pp. 1037–1045.

[12] Hirsch, C., *Numerical Computation of Internal and External Flows*, 1st ed., Vol. 2, Wiley, New York, 1992, pp. 132–223.

[13] Ashcroft, G., and Zhang, X., "Optimized Prefactored Compact Schemes," *Journal of Computational Physics*, Vol. 190, No. 2, 2003, pp. 459–477. doi:10.1016/S0021-9991(03)00293-6

[14] Gustafsson, B., "The Convergence Rate for Difference Approximations to Mixed Initial Boundary Value Problems," *Mathematics of Computation*, Vol. 29, No. 130, 1975, pp. 396–406.

[15] Hu, F. Q., Hussani, M. Y., and Manthey, J., "Low-Dissipation and Low-Dispersion Runge–Kutta Schemes for Computational Acoustics," NASA CR-195022, 1994.

[16] Tam, C. K. W., and Kurbatskii, K. A., "A Wavenumber Based Extrapolation and Interpolation Method for Use in Conjunction with High-Order Finite Difference Schemes," *Journal of Computational Physics*, Vol. 157, No. 2, 2000, pp. 588–617. doi:10.1006/jcph.1999.6393

[17] Sherer, S. E., and Scott, J. N., "Comparison of Highly Accurate Interpolation Methods," AIAA Paper 2001-0282, 2001.

[18] Carnahan, B., Luther, H., and Wilkes, J. O., *Applied Numerical Methods*, Wiley, New York, 1969.

[19] Visbal, M. R., and Gaitonde, D. V., "On the Use of Higher-Order Finite-Difference Schemes on Curvilinear and Deforming Meshes," *Journal of Computational Physics*, Vol. 181, No. 1, 2002, pp. 155–185. doi:10.1006/jcph.2002.7117

[20] Richards, S. K., Zhang, X., Chen, X. X., and Nelson, P. A., "The Evaluation of Nonreflecting Boundary Conditions for Duct Acoustic Computation," *Journal of Sound and Vibration*, Vol. 270, No. 3, 2004, pp. 539–557. doi:10.1016/j.jsv.2003.09.042

[21] Hardin, J. C., Ristorcelli, J. R., and Tam, C. K., "ICASE/LaRC Workshop on Benchmark Problems in Computational Aeroacoustics," NASA CP-3300, 1995.

[22] Tam, C. K. W., and Hardin, J. C., "Proceedings of the Second Computational Aeroacoustics Workshop on Benchmark Problems," NASA CP-3352, 1997.

[23] Kim, J. W., and Lee, D. J., "Generalized Characteristic Boundary Conditions for Computational Aeroacoustics, Part 2," *AIAA Journal*, Vol. 42, No. 1, 2004, pp. 47–55. doi:10.2514/1.9029

W. Anderson
Associate Editor